Supporting Information

Transition from Dion Jacobson Hybrid Layered Double Perovskites to 1D Perovskites for Ultraviolet to Visible Photodetection

Arnab Mandal,[1] Shresth Gupta,[1] Supriti Dutta,[2] Swapan K. Pati,[2] Sayan Bhattacharyya[1,*]

[1]*Department of Chemical Sciences and Centre for Advanced Functional Materials, Indian Institute of Science Education and Research (IISER) Kolkata, Mohanpur - 741246, India*
[2]*Theoretical Sciences Unit, School of Advanced Materials, Jawaharlal Nehru Centre for Advanced Scientific Research (JNCASR), Bangalore 560064, India*

*Email for correspondence: sayanb@iiserkol.ac.in

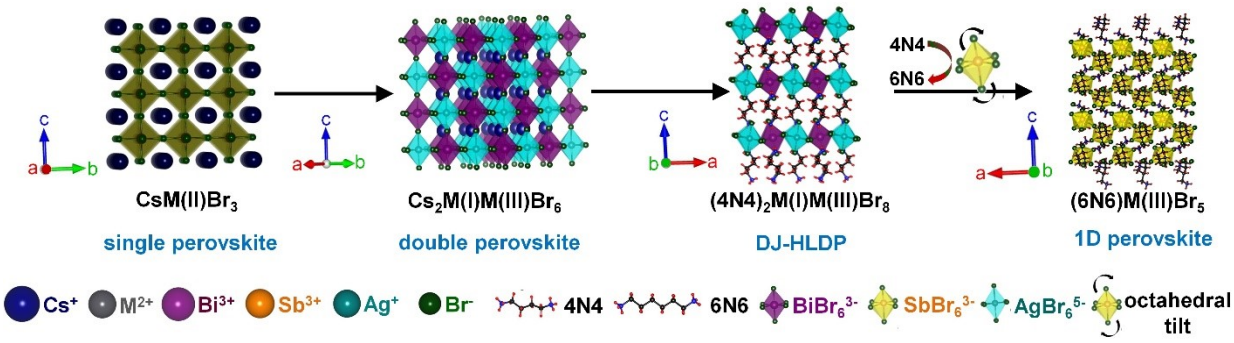

Figure S1. Schematic representation of the evolution of DJ-HLDP and 1D perovskites.

Table S1. Elongation factors of the octahedra in $(4N4)_2AgBiBr_8$, $(4N4)_2AgSbBr_8$, $(6N6)_2AgBiBr_8$ and $(6N6)SbBr_5$.

Perovskite	λ_{oct} (BBr_6^{3-})	λ_{oct} ($AgBr_6^{5-}$)	σ^2 (BBr_6^{3-})	σ^2 ($AgBr_6^{5-}$)
$(4N4)_2AgBiBr_8$	2.1×10^{-6}	5.4×10^{-3}	1.1	7.2
$(4N4)_2AgSbBr_8$	4.5×10^{-6}	4.9×10^{-3}	1.3	10.5
$(6N6)_2AgBiBr_8$	1.6×10^{-6}	5.4×10^{-3}	5.1	8.4
$(6N6)SbBr_5$	3.8×10^{-3}	-	8.6	-

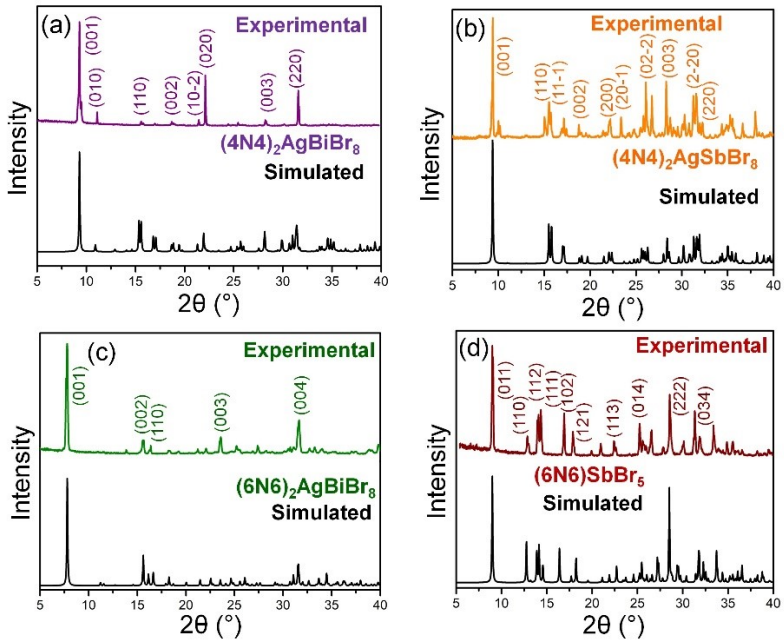

Figure S2. Comparison of PXRD patterns with the simulated patterns from SCXRD data for (a) $(4N4)_2AgBiBr_8$, (b) $(4N4)_2AgSbBr_8$,(c) $(6N6)_2AgBiBr_8$, and (d) $(6N6)SbBr_5$. The SCXRD data of $(4N4)_2AgBiBr_8$ is in accordance with the reported $(BDA)_2AgBiBr_8$ (*J. Am. Chem. Soc.* **2019**, *141*, 19099-19109).

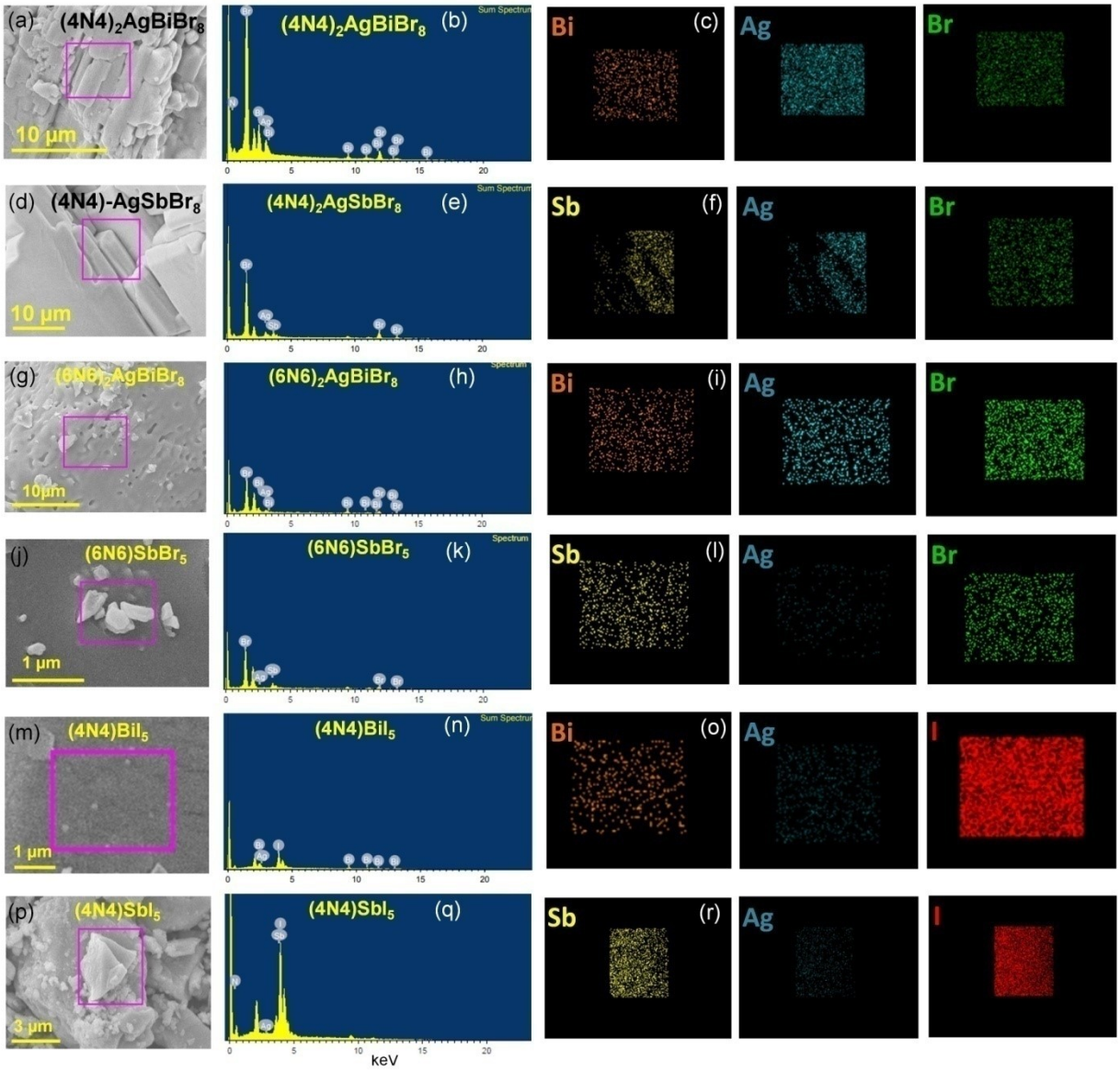

Figure S3. FESEM images, EDAX spectra and corresponding elemental mapping of (a,b,c) $(4N4)_2AgBiBr$, (d,e,f) $(4N4)_2AgSbBr_8$, (g,h,i) $(6N6)_2AgBiBr_8$, (j,k,l) $(6N6)SbBr_5$, (m,n,o) (4N4)-BiI and (p,q,r) (4N4)-SbI.

Table S2. Elemental analysis of $(4N4)_2AgBiBr_8$, $(4N4)_2AgSbBr_8$, $(6N6)_2AgBiBr_8$, $(6N6)SbBr_5$, (4N4)-BiI and (4N4)-SbI.

Perovskite	Bi (at%)	Sb (at%)	Ag (at%)	Br (at%)	I (at%)
$(4N4)_2AgBiBr_8$	10.3	-	9.1	80.6	-
$(4N4)_2AgSbBr_8$	-	9.6	8.7	81.6	-
$(6N6)_2AgBiBr_8$	11.5	-	8.6	79.9	-
$(6N6)SbBr_5$	-	15.8	-	84.2	-
(4N4)-BiI	12.8	-	-	-	87.1
(4N4)-SbI	-	16.9	-	-	83.1

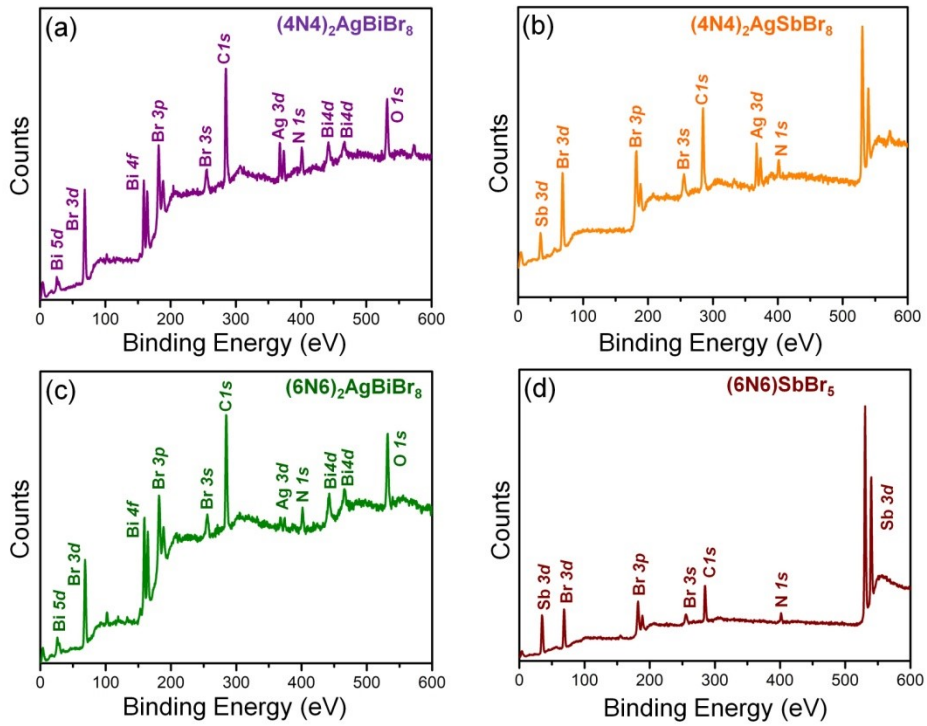

Figure S4. XPS survey scan for (a) $(4N4)_2AgBiBr_8$, (b) $(4N4)_2AgSbBr_8$,(c) $(6N6)_2AgBiBr_8$, and (d) $(6N6)SbBr_5$.

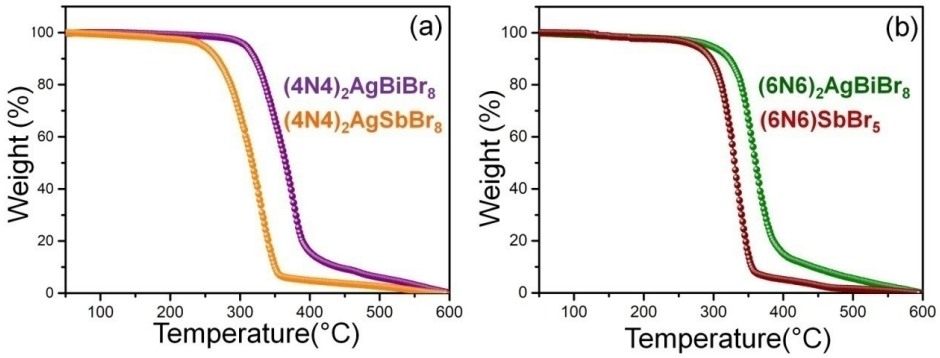

Figure S5. TGA plots for (a) $(4N4)_2AgBiBr_8$, and $(4N4)_2AgSbBr_8$, and (b) $(6N6)_2AgBiBr_8$, and $(6N6)SbBr_5$.

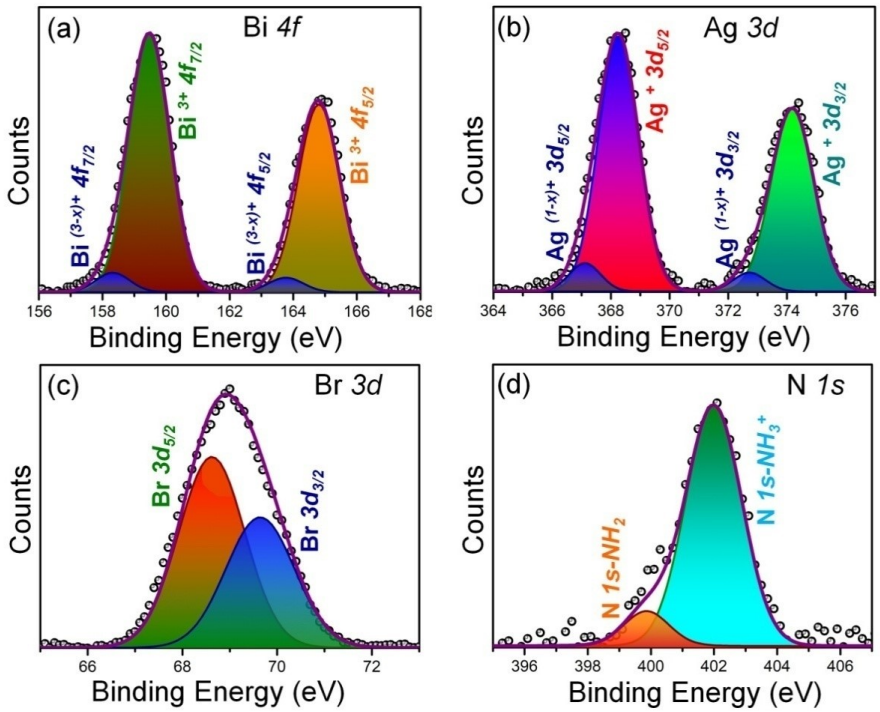

Figure S6. XPS plots of (a) Bi *4f*, (b) Ag *3d*, (c) Br *3d*, and (d) N *1s* levels of $(4N4)_2AgBiBr_8$.

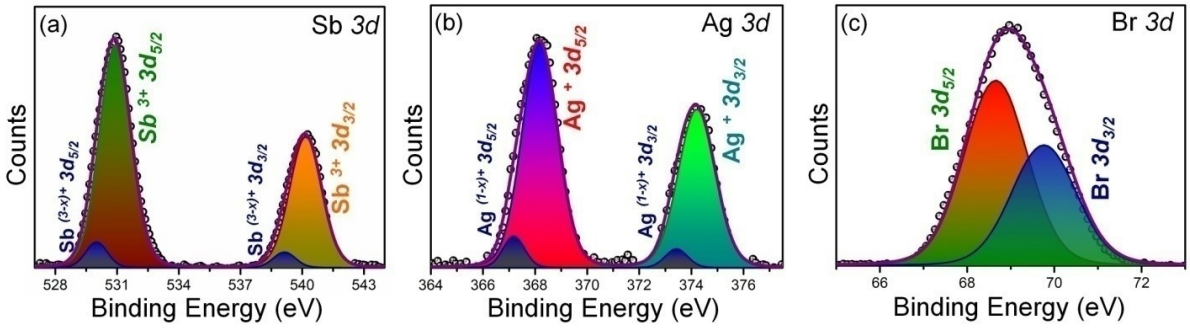

Figure S7. XPS plots of (a) Sb *3d*, (b) Ag *3d*, and (c) Br *3d* levels of $(4N4)_2AgSbBr_8$.

Table S3. Fitted XPS parameters of $(4N4)_2AgBiBr_8$ and $(4N4)_2AgSbBr_8$.

a. XPS of Bi *4f* level of Bi^{3+} state

Perovskite	$4f_{7/2}$ B.E. (eV)	Area $4f_{7/2}$	$4f_{5/2}$ B.E. (eV)	Area $4f_{5/2}$
$(4N4)_2AgBiBr_8$	159.5	4768	164.8	3546

b. XPS of Bi *4f* level of $Bi^{(3-x)+}$ state

Perovskite	$4f_{7/2}$ B.E. (eV)	Area $4f_{7/2}$	$4f_{5/2}$ B.E. (eV)	Area $4f_{5/2}$
$(4N4)_2AgBiBr_8$	158.3	299.9	163.8	229

c. XPS of Sb *3d* level of Sb^{3+} state

Perovskite	$3d_{5/2}$ B.E. (eV)	Area $3d_{5/2}$	$3d_{3/2}$ B.E. (eV)	Area $3d_{3/2}$
$(4N4)_2AgSbBr_8$	530.9	12517	540.2	7429

d. XPS of Sb *3d* level of $Sb^{(3-x)+}$ state

Perovskite	$3d_{5/2}$ B.E. (eV)	Area $3d_{5/2}$	$3d_{3/2}$ B.E. (eV)	Area $3d_{3/2}$
$(4N4)_2AgSbBr_8$	530	979	539.1	611

e. Relative ratio of M^{3+} and $M^{(3-x)+}$ states (M = Bi and Sb)

Perovskite	Total area of M^{3+}	Total area of $M^{(3-x)+}$	Area $M^{(3-x)+}$/Area M^{3+}
$(4N4)_2AgBiBr_8$	8314	528	0.06
$(4N4)_2AgSbBr_8$	19946	1590	0.08

f. XPS of Ag *3d* level of Ag^{+} state

Perovskite	$3d_{5/2}$ B.E. (eV)	Area $3d_{5/2}$	$3d_{3/2}$ B.E. (eV)	Area $3d_{3/2}$
$(4N4)_2AgBiBr_8$	368.2	2799	374.2	2114
$(4N4)_2AgSbBr_8$	368.2	3473	374.2	2552

g. XPS of Ag *3d* level of $Ag^{(1-x)+}$ state

Perovskite	$3d_{5/2}$ B.E. (eV)	Area $3d_{5/2}$	$3d_{3/2}$ B.E. (eV)	Area $3d_{3/2}$
$(4N4)_2AgBiBr_8$	367.1	241	372.7	166
$(4N4)_2AgSbBr_8$	367.2	296	372.7	183

h. Relative ratio of Ag^{+} and $Ag^{(1-x)+}$ states

Perovskite	Total area of Ag^{+}	Total area of $Ag^{(1-x)+}$	Area $Ag^{(1-x)+}$/Area Ag^{+}
$(4N4)_2AgBiBr_8$	4913	407	0.08
$(4N4)_2AgSbBr_8$	6025	479	0.08

i. XPS of Br *3d* level

Perovskite	$3d_{5/2}$ B.E. (eV)	Area$3d_{5/2}$	$3d_{3/2}$ B.E. (eV)	Area $3d_{3/2}$	Area $3d_{5/2}$ / Area $3d_{3/2}$
$(4N4)_2AgBiBr_8$	68.6	4449	69.6	3164	1.4
$(4N4)_2AgSbBr_8$	68.6	6074	69.7	4075	1.5

j. XPS of N *1s* level

Perovskite	NH_2 B.E. (eV)	AreaNH_2	NH_3^+ B.E. (eV)	Area NH_3^+	Area NH_3^+/ Area NH_2
$(4N4)_2AgBiBr_8$	399.8	203	401.9	1912	9.4

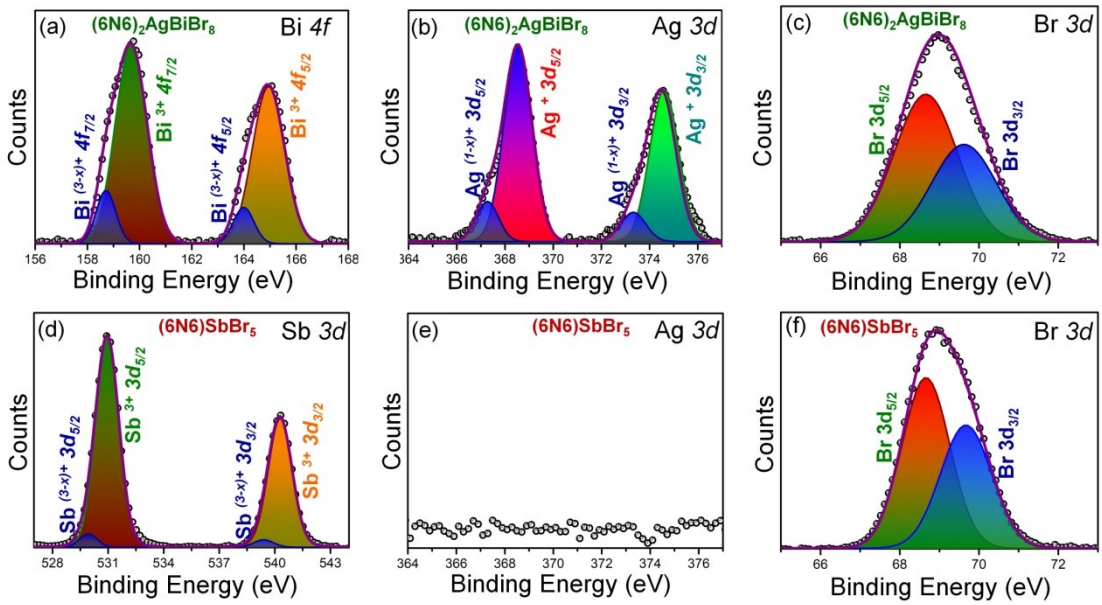

Figure S8. XPS plots of (a) Bi *4f*, (b) Ag *3d*, and (c) Br *3d* levels of $(6N6)_2AgBiBr_8$, and (d) Sb *3d*, (e) Ag *3d*, and (f) Br *3d* levels of $(6N6)SbBr_5$.

Table S4. Fitted XPS parameters of $(6N6)_2AgBiBr_8$ and $(6N6)SbBr_5$.

a. XPS of Bi *4f* level of Bi^{3+} state

Perovskite	$4f_{7/2}$ B.E. (eV)	Area $4f_{7/2}$	$4f_{5/2}$ B.E. (eV)	Area $4f_{5/2}$
$(6N6)_2AgBiBr_8$	159.6	3615	164.9	2893

b. XPS of Bi *4f* level of $Bi^{(3-x)+}$ state

Perovskite	$4f_{7/2}$ B.E. (eV)	Area $4f_{7/2}$	$4f_{5/2}$ B.E. (eV)	Area $4f_{5/2}$
$(6N6)_2AgBiBr_8$	158.7	587	163.9	424

c. XPS of Sb *3d* level of Sb^{3+} state

Perovskite	$3d_{5/2}$ B.E. (eV)	Area $3d_{5/2}$	$3d_{3/2}$ B.E. (eV)	Area $3d_{3/2}$
$(6N6)SbBr_5$	530.9	28730	540.3	18357

d. XPS of Sb *3d* level of $Sb^{(3-x)+}$ state

Perovskite	$3d_{5/2}$ B.E. (eV)	Area $3d_{5/2}$	$3d_{3/2}$ B.E. (eV)	Area $3d_{3/2}$
$(6N6)SbBr_5$	529.9	1382	539.4	897

e. Relative ratio of M^{3+} and $M^{(3-x)+}$ states (M = Bi and Sb)

Perovskite	Total area of M^{3+}	Total area of $M^{(3-x)+}$	Area $M^{(3-x)+}$/Area M^{3+}
$(6N6)_2AgBiBr_8$	6508	1011	0.13
$(6N6)SbBr_5$	47087	2279	0.05

f. XPS of Ag *3d* level of Ag^{+} state

Perovskite	$3d_{5/2}$ B.E. (eV)	Area $3d_{5/2}$	$3d_{3/2}$ B.E. (eV)	Area $3d_{3/2}$
$(6N6)_2AgBiBr_8$	368.4	686.5	374.4	538.2
$(6N6)SbBr_5$	-	-	-	-

g. XPS of Ag *3d* level of $Ag^{(1-x)+}$ state

Perovskite	$3d_{5/2}$ B.E. (eV)	Area $3d_{5/2}$	$3d_{3/2}$ B.E. (eV)	Area $3d_{3/2}$
$(6N6)_2AgBiBr_8$	367.3	111	373.2	90
$(6N6)SbBr_5$	-	-	-	-

h. Relative ratio of Ag^{+} and $Ag^{(1-x)+}$ states

Perovskite	Total area of Ag^{+}	Total area of $Ag^{(1-x)+}$	Area $Ag^{(1-x)+}$/Area Ag^{+}
$(6N6)_2AgBiBr_8$	1225	201	0.14
$(6N6)SbBr_5$	-	-	-

i. XPS of Br *3d* level

Perovskite	$3d_{5/2}$ B.E. (eV)	Area$3d_{5/2}$	$3d_{3/2}$ B.E. (eV)	Area $3d_{3/2}$	Area $3d_{5/2}$ / Area $3d_{3/2}$
$(6N6)_2AgBiBr_8$	68.6	4087	69.6	2768	1.5
$(6N6)SbBr_5$	68.7	3857	69.7	2981	1.3

Table S5. Photophysical parameters of $(4N4)_2AgBiBr_8$, $(4N4)_2AgSbBr_8$, $(6N6)_2AgBiBr_8$ and $(6N6)SbBr_5$.

Perovskite	PL peak (nm)	Stokes shift (nm)	FWHM (nm)	Direct bandgap (eV)	Indirect bandgap (eV)
$(4N4)_2AgBiBr_8$	522.1	50.8	57.9	2.53	2.42
$(4N4)_2AgSbBr_8$	490.8	40.6	51.6	2.73	2.58
$(6N6)_2AgBiBr_8$	517.7	52.3	68.2	2.61	2.49
$(6N6)SbBr_5$	510.2	46.1	56.7	2.57	2.46

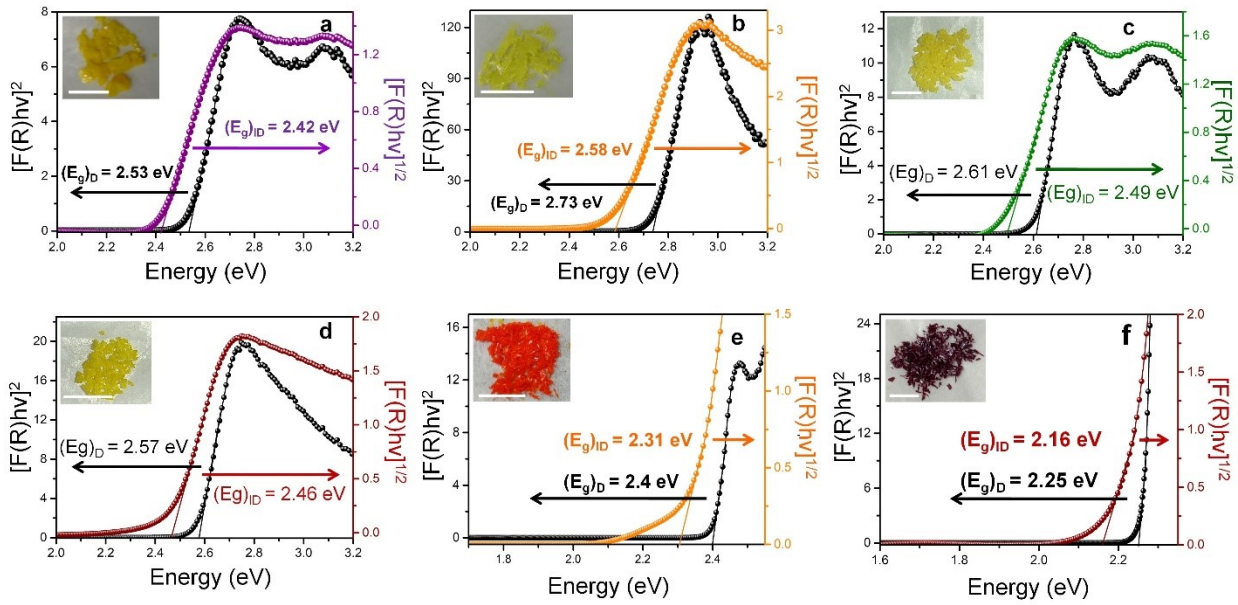

Figure S9. Direct $[(E_g)_D]$ and indirect $[(E_g)_{ID}]$ bandgap estimation by Kubelka−Munk transformed data for (a) $(4N4)_2AgBiBr_8$, (b) $(4N4)_2AgSbBr_8$, (c) $(6N6)_2AgBiBr_8$, (d) $(6N6)SbBr_5$, (e) (4N4)-BiI, and (f) (4N4)-SbI. The six insets show the digital images of the corresponding perovskite crystals. Scale bar = 1 cm.

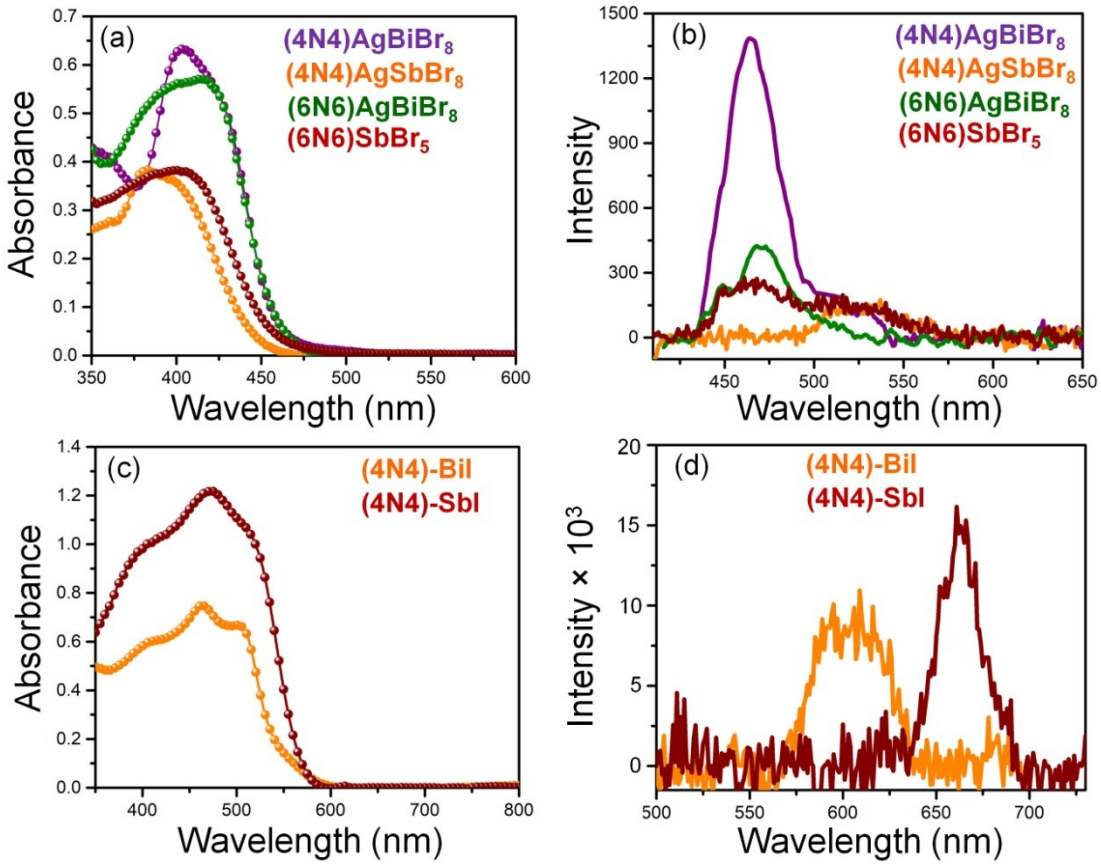

Figure S10. (a) Absorption, and (b) PL spectra of $(4N4)_2AgBiBr_8$, $(4N4)_2AgSbBr_8$, $(6N6)_2AgBiBr_8$ and $(6N6)SbBr_5$ films. (c) Absorption, and (d) PL spectra of (4N4)-BiI and (4N4)-SbI films.

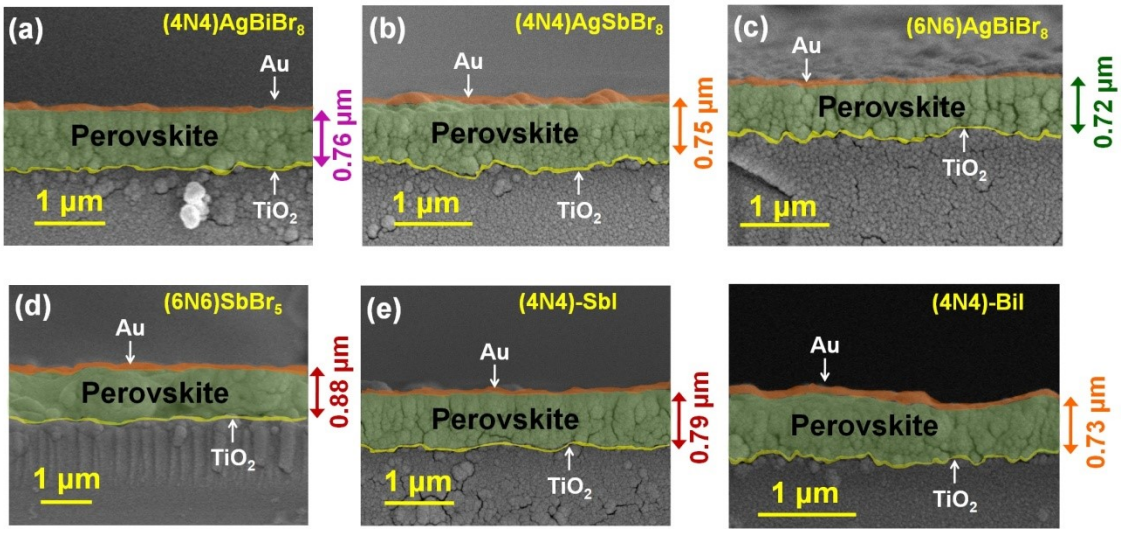

Figure S11. Cross-sectional FESEM images of (a) $(4N4)_2AgBiBr_8$, (b) $(4N4)_2AgSbBr_8$, (c) $(6N6)_2AgBiBr_8$, (d) $(6N6)SbBr_5$, (e) (4N4)-SbI, and (f) (4N4)-BiI photodetector devices.

Table S6. Absorption coefficient of the DJ HLDPs and 1D perovskites.

Perovskite	$(4N4)_2AgBiBr_8$	$(4N4)_2AgSbBr_8$	$(6N6)_2AgBiBr_8$	$(6N6)SbBr_5$	(4N4)BiI	(4N4)SbI
Absorption Coefficient (cm^{-1})	8.3×10^3	5.1×10^3	7.9×10^3	4.3×10^3	1×10^4	1.5×10^4

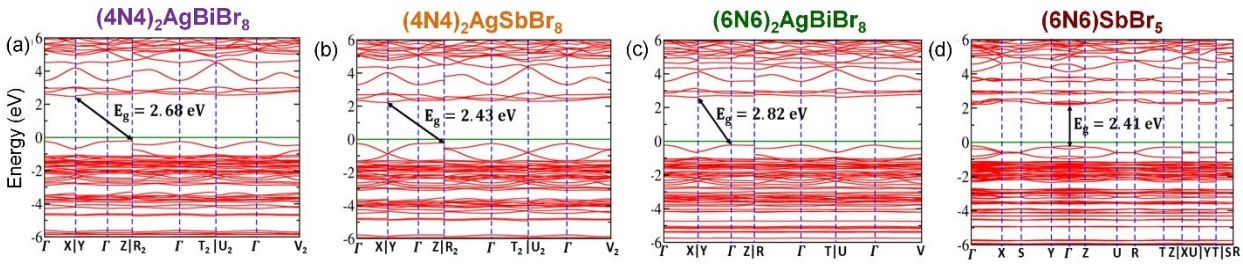

Figure S12. Electronic band structures without SOC for (a) $(4N4)_2AgBiBr_8$, (b) $(4N4)_2AgSbBr_8$, (c) $(6N6)_2AgBiBr_8$, and (d) $(6N6)SbBr_5$.

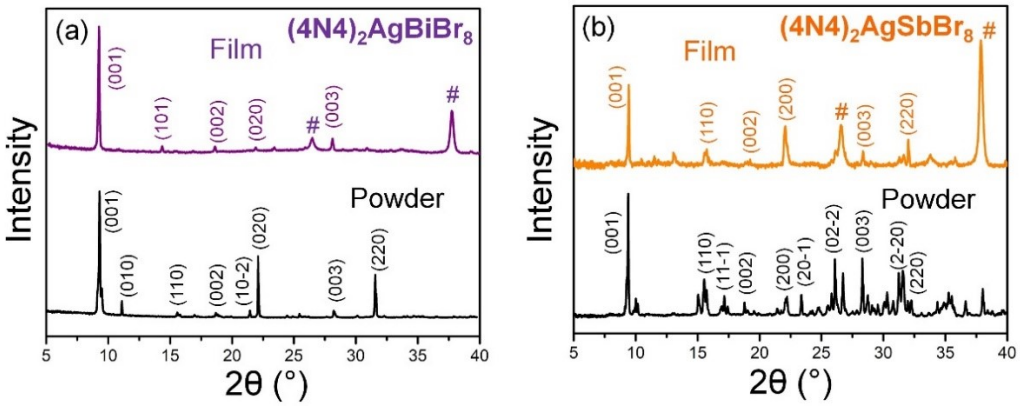

Figure S13. Comparative PXRD patterns of the crystals and films of (a) $(4N4)_2AgBiBr_8$ and (b) $(4N4)_2AgSbBr_8$. # denotes the reflections from the FTO coated glass substrate.

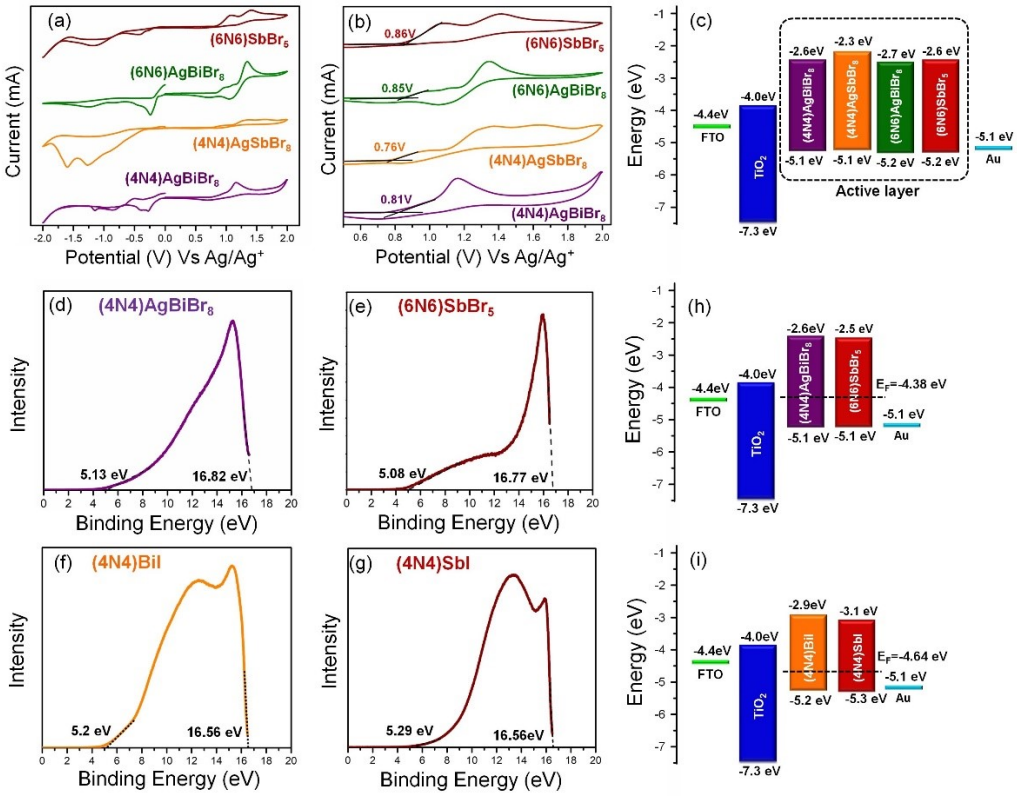

Figure S14. (a, b) Cyclic voltammetry (CV) plots of $(4N4)_2AgBiBr_8$, $(4N4)_2AgSbBr_8$, $(6N6)_2AgBiBr_8$ and $(6N6)SbBr_5$. (c) Band energy diagram of the perovskites with respect to FTO, TiO_2 and Au (based on the CV results). UV photoelectron spectra of (d) $(4N4)_2AgBiBr_8$, (e) $(6N6)SbBr_5$, (f) (4N4)-BiI, and (g) (4N4)-SbI. Energy band diagrams of different layers of the photodetector devices (based on UPS results) with the (h) representative bromide HLDPs, and (i) 1D iodide perovskites.

The highest occupied molecular orbital (HOMO) energy level of the bromide HLDPs were measured from cyclic voltammogram (CV) by the expression: $E_{HOMO} = -(4.8 - E_{ferrocene}^{1/2} + E_{Onset}^{Ox})$ eV and lowest unoccupied molecular orbital (LUMO) was calculated as: $E_{LUMO} = (E_{HOMO} + E_g)$ eV, where E_{Onset}^{Ox} is the onset of the first oxidation peak, $E_{ferrocene}^{1/2}$ is the half-wave potential of ferrocene/ferrocenium redox couple, and E_g is the optical bandgap (Figure S14a,b). CV experiments could not be performed for the iodide 1D perovskites since they degrade in the polar electrolyte while recording the CV plots. Ultraviolet photoelectron spectroscopy (UPS) was employed to determine the Fermi energy levels (E_F) and energy bands of the bromide and iodide perovskites where E_F was estimated to be -4.38 and -4.64 eV, respectively indicating their *p*-type nature (Figure S14d-g). E_F and HOMO are determined from the intercepts to the binding energy axis. The intercept at lower binding energy region determines the HOMO, whereas E_F is calculated as: $E_F = (21.2 - x)$ eV, where 21.2 eV is the energy of the incident photon and x is the intercept at higher binding energy. The LUMO is calculated as $E_{LUMO} = (E_{HOMO} + E_g)$ eV. The UPS results match well with the CV data. The energy diagram of the photodetector devices consisting of the HOMO and LUMO levels of the perovskite active layers, electron transport layer (TiO_2) and Fermi energy of the FTO and Au electrodes show a facile carrier transport from the active layer to the conducting electrodes (Figure S14c,h,i).

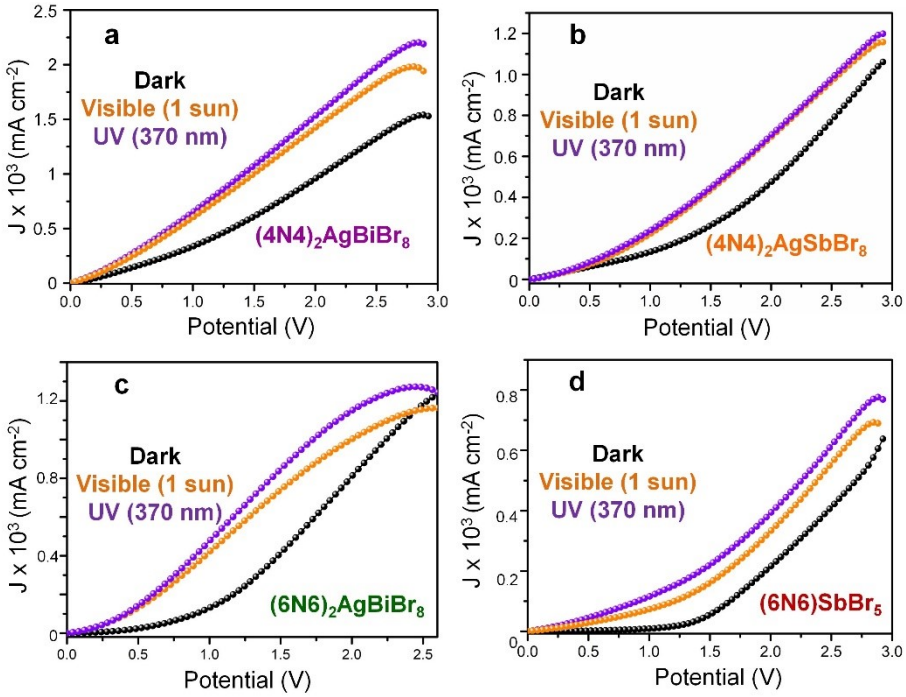

Figure S15. Potential-biased photodetector performance. *J-V* plots under 1 sun visible light and 370 nm UV light for (a) $(4N4)_2AgBiBr_8$, (b) $(4N4)_2AgSbBr_8$, (c) $(6N6)_2AgBiBr_8$, and (d) $(6N6)SbBr_5$.

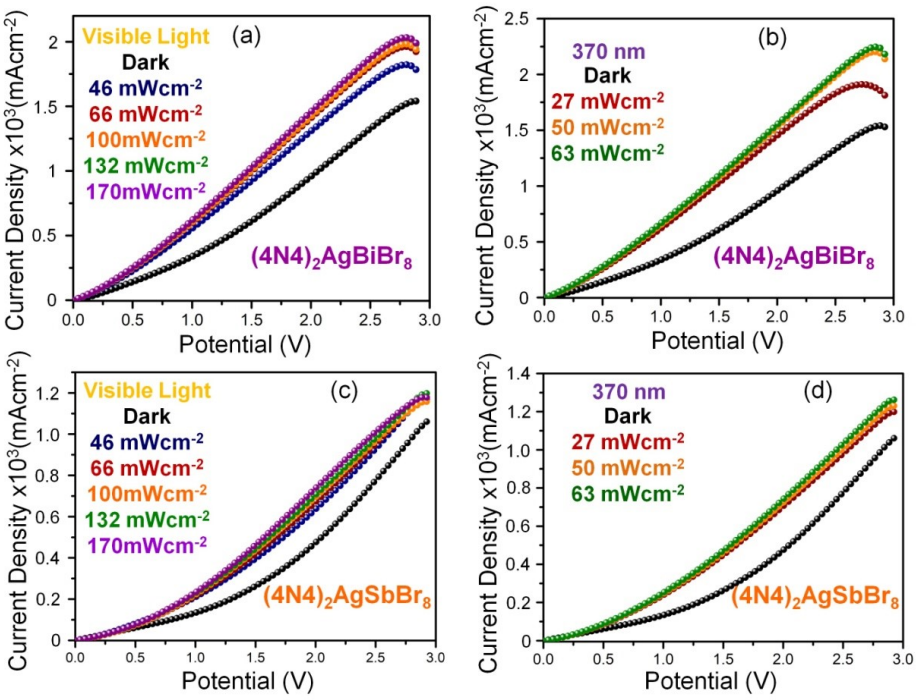

Figure S16. *J-V* plots of (a, b) $(4N4)_2AgBiBr_8$ and (c, d) $(4N4)_2AgSbBr_8$ devices under illumination by visible and UV light of different intensities.

Table S7. Highest obtained responsivity (*R*), detectivity (*D*) and *EQE* of the photodetectors under applied bias in presence of both visible light and UV light of a particular wavelength.

Perovskite	*R* (mAW^{-1})	*D* (Jones)	*EQE* (%)
	Visible light (46 $mWcm^{-2}$)		
$(4N4)_2AgBiBr_8$	7.7 ± 0.1 (2.5 V)	-	-
$(4N4)_2AgSbBr_8$	3.4 ± 0.1 (2 V)	-	-
$(6N6)_2AgBiBr$	6.1 ± 0.3 (1.5 V)	-	-
$(6N6)SbBr_5$	2.1 ± 0.1 (2.5 V)	-	-
	370 nm (27 $mWcm^{-2}$)		
$(4N4)_2AgBiBr_8$	18.8 ± 0.2 (2.5 V)	1.1 (± 0.02) × 10^9 (1.5 V)	6360 ± 58 (2.5 V)
$(4N4)_2AgSbBr_8$	8.6 ± 0.2 (2 V)	0.8 (± 0.02) × 10^9 (1.5 V)	2880 ± 25 (2 V)
$(6N6)_2AgBiBr$	16.1 ± 0.2 (1.5 V)	1.9 (± 0.1) × 10^9 (1 V)	5418 ± 90 (1.5 V)
$(6N6)SbBr_5$	4.1 ± 0.1 (2.5 V)	1 (± 0.1) × 10^9 (1 V)	1333 ± 23 (2.5V)
	485nm (4.7 $mWcm^{-2}$)		
(4N4)-BiI	1.6 (± 0.1) (3 V)	1.2 (± 0.1) × 10^9 (2 V)	405 ± 5 (3 V)
(4N4)-SbI	6.1 (± 0.2) (3 V)	1.3 (± 0.1) × 10^9 (2.5 V)	1560 ± 15 (3 V)

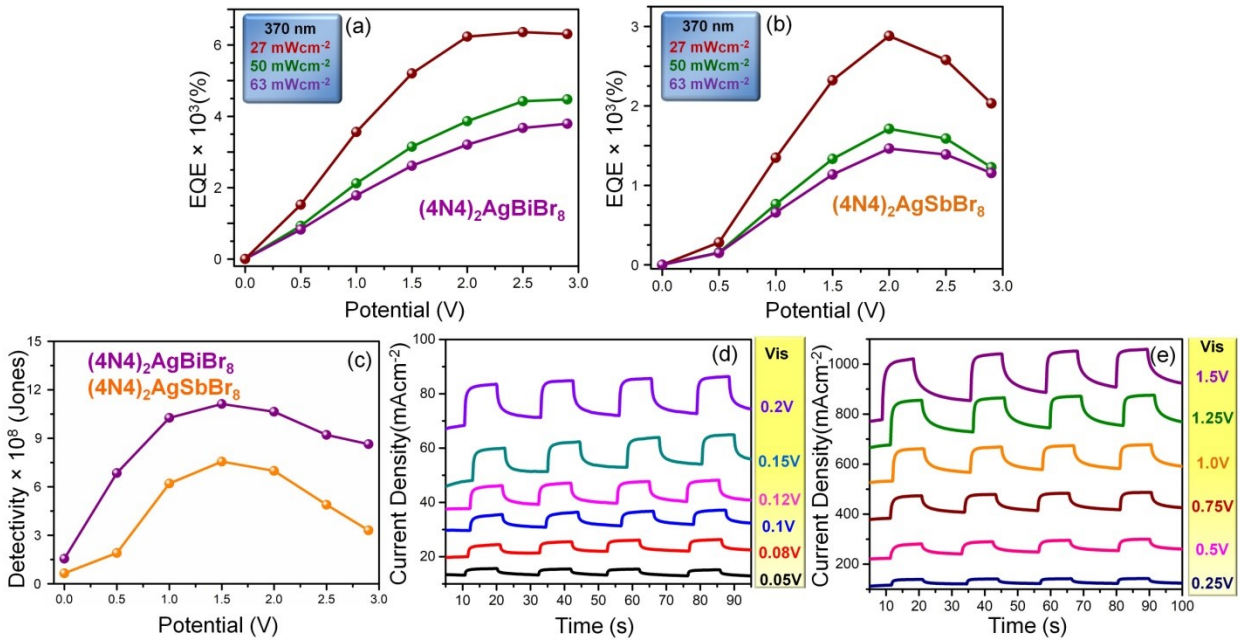

Figure S17. Variation of *EQE* with applied potential for (a) $(4N4)_2AgBiBr_8$ and (b) $(4N4)_2AgSbBr_8$ in the presence of UV light with different intensities. (c) Variation of detectivity with applied potential for $(4N4)_2AgBiBr_8$ and $(4N4)_2AgSbBr_8$. (d,e) Chronoamperometry plots of $(4N4)_2AgBiBr_8$ at different potentials (0.05 to 1.5 V) in the presence of 1 sun illumination.

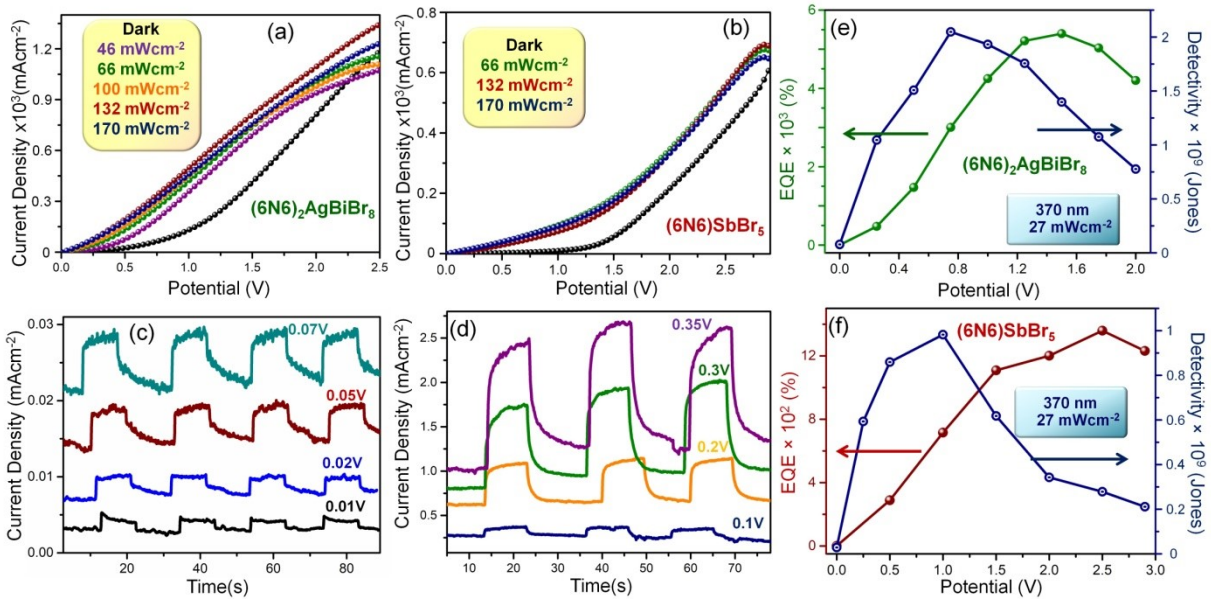

Figure S18. *J-V* plots of (a) $(6N6)_2AgBiBr_8$ and (b) $(6N6)SbBr_5$ in presence of visible light of different intensities. (c) Chronoamperometry plots of $(6N6)_2AgSbBr_8$ at different potentials (0.01 to 0.35 V) in presence of 1 sunlight. *EQE* and detectivity variation with applied potential for (e) $(6N6)_2AgBiBr_8$ and (f) $(6N6)SbBr_5$ devices in the presence of UV light.

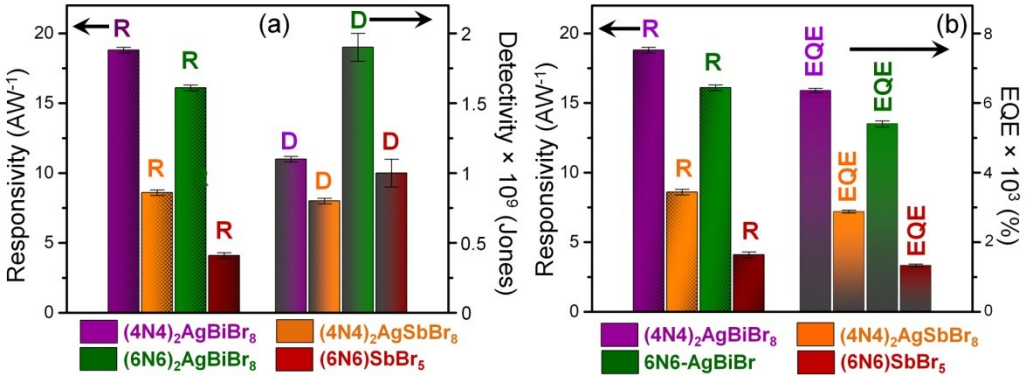

Figure S19. Bar plots of the highest (a) responsivity (*R*) and detectivity (*D*),and (b) *R* and *EQE* for all the bromide DJ-HLDP and 1D $(6N6)SbBr_5$underpotential-bias.

Table S8. Highest obtained responsivity (*R*), detectivity (*D*) and *EQE* of all the bromide photodetectors under potential-bias in the presence of 360 nm UV light.

Material	*R* (AW^{-1})	*D* (Jones)	*EQE* (%)
$(4N4)_2AgBiBr_8$	18.8 ± 0.2 (2.5 V)	1.1 (± 0.02) × 10^9 (1.5 V)	6360 ± 58 (2.5 V)
$(4N4)_2AgSbBr_8$	8.6 ± 0.2 (2 V)	0.8 (± 0.02) × 10^9 (1.5 V)	2880 ± 25 (2 V)
$(6N6)_2AgBiBr_8$	16.1 ± 0.2 (1.5 V)	1.9 (± 0.1) × 10^9 (1 V)	5418 ± 90 (1.5 V)
$(6N6)SbBr_5$	4.1 ± 0.1 (2.5 V)	1 (± 0.1) × 10^9 (1 V)	1333 ± 23 (2.5 V)

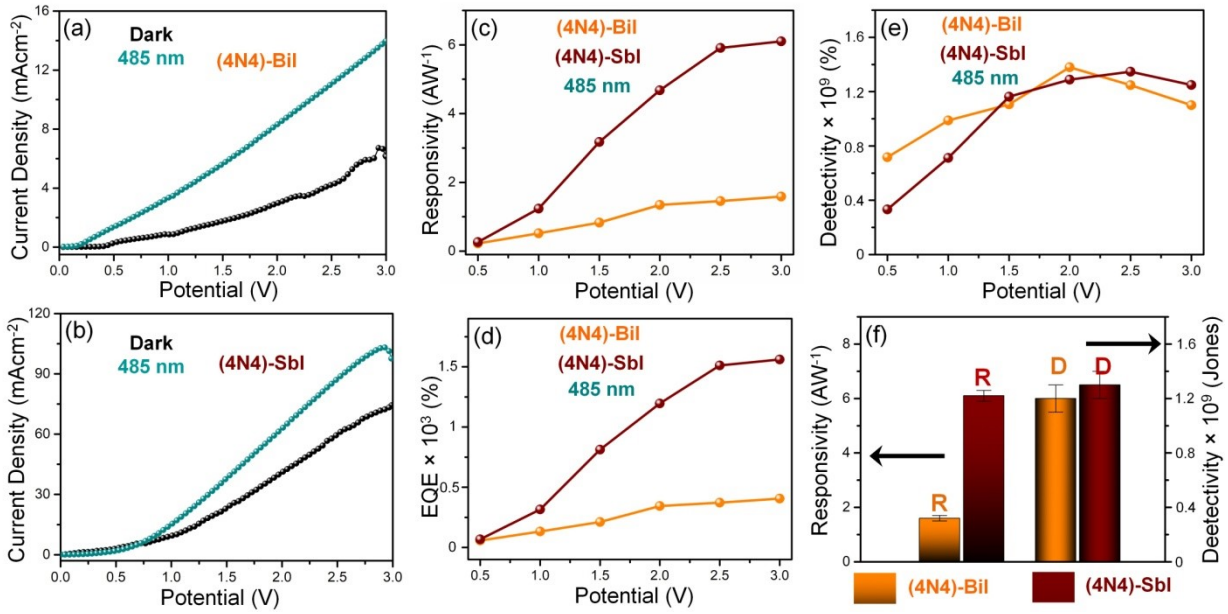

Figure S20. Photodetector performance of (4N4)-BiI and (4N4)-SbI devices. (a,b) *J-V* plots in the presence and absence of illumination (1 sun and 470 nm light). Variation of (c) responsivity (*R*), (d) *EQE* and (e) detectivity (*D*) with applied potentialin presence of 485 nm illumination. (f) Bar plots of maximum obtained *R* and *D* values under 485 nm illumination.

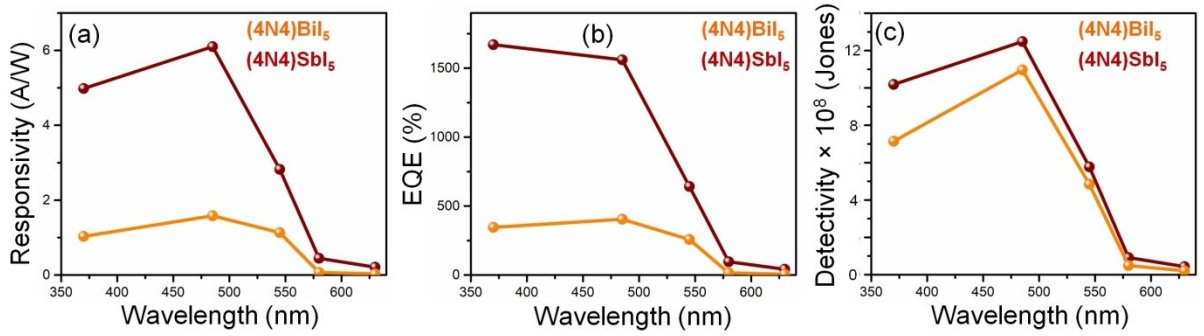

Figure S21. Wavelength-dependent variation of (a) responsivity (*R*), (b) *EQE* and (c) detectivity (*D*) of (4N4)-SbI and (4N4)-BiI photodetector devices.

Table S9. Comparison of photodetection of the DJ-HLDP devices with the reported HLDPs operating under potential bias.

HLDP photodetectors	Bias (V)	RT/FT (ms)	*R* (AW^{-1})	*D* (Jones)	Ref.
(*n*-propylammonium)$_2$CsAgBiBr$_7$	5	0.141/0.255	0.05	2.3×10^{11}	S1
(isopentylammonium)$_2$CsAgBiBr$_7$	10	0.2/0.4	-	-	S2
[(R)-β-(MPA)]$_4$AgBiI$_8$; [(S)-β-(MPA)]$_4$AgBiI$_8$ (β-MPA = methylphenethylammonium)	5	580/960	2×10^{-5}	1.2×10^{7}	S3
(4N4)$_2$AgBiBr$_8$	2.5	98/95	18.8 ± 0.2	1.1 (± 0.02) $\times 10^{9}$	This work
(4N4)$_2$AgSbBr$_8$	2	104/98	8.6 ± 0.2	0.8 (± 0.02) $\times 10^{9}$	This work
(6N6)$_2$AgBiBr$_8$	1.5	100/99	16.1± 0.2	1.9 (± 0.1) $\times 10^{9}$	This work

Table S10. Comparison of photodetection parameters of the DJ-HLDP devices with the reported lead-containing DJ-perovskites operating under potential bias.

DJ-perovskite photodetectors	Bias (V)	*R* (AW^{-1})	*EQE* (%)	*D* (Jones)	Ref.
EDA(MA)$_{n-1}$Pb$_n$I$_{3n+1}$ [EDA = ethylenediammonium; MA = methylammonium]	2	0.125	30	7.1×10^{10}	S4
(2meptH$_2$)(MA)Pb$_2$I$_7$ [2meptH$_2$ = 2-methyl-1,5-diaminopentane]	10	13	3100	-	S5
(3AMPY)(FA)Pb$_2$I$_7$ [3AMPY = 3(aminomethyl)pyridinium FA = formamidinium]	10	0.2	40	6×10^{12}	S6
(2meptH$_2$)CsPb$_2$Br$_7$	10	0.1	40	10^{9}	S7
(4-AMP)Cs$_2$Pb$_3$Br$_{10}$ [4-AMP = (aminomethyl)piperidinium]	10	0.02	-	6.5×10^{10}	S8
(HDA)CsPb$_2$Br$_7$ [HDA = 1,6-hexamethylenediammonium]	10	2.1×10^{-4}	0.06	1.5×10^{9}	S9
[DMPDA]PbI$_4$ [DMPDA = N,N-dimethyl-1,3-propanediamine, C$_5$H$_{14}$N$_2$)]	1.5	0.074	20.2	1.1×10^{12}	S10
(4N4)$_2$AgBiBr$_8$	2.5	18.8 ± 0.2	6360 ± 58	1.1 (± 0.02) $\times 10^{9}$	This work
(4N4)$_2$AgSbBr$_8$	2	8.6 ± 0.2	2880 ± 25	0.8 (± 0.02) $\times 10^{9}$	This work
(6N6)$_2$AgBiBr$_8$	1.5	16.1 ± 0.2	5418 ± 90	1.9 (± 0.1)	This

				$\times 10^9$	work

Table S11. Comparison of photodetection parameters of the DJ-HLDP devices with the reported $Cs_2AgBiBr_6$ double perovskite systems operating under potential bias.

Perovskite photodetectors	Bias (V)	*R* (AW^{-1})	*EQE* (%)	*D* (Jones)	Ref.
Au/$Cs_2AgBiBr_6$ Film/Au	5	7.01	2146	5.6×10^{11}	S11
2D $Cs_2AgBiBr_6$/WS_2/graphene	4	0.52	14.7	1.5×10^{13}	S12
Au/$Cs_2AgBiBr_6$ single crystal/Au	10	4.88	1100	1.2×10^{13}	S13
Au/ $Cs_2AgBiBr_6$ single crystal/Au	5	$\sim 10^{-3}$	-	1.4×10^9	S14
Au/ 2D-$Cs_2AgBiBr_6$ /Au	5	54.6	-	1.4×10^{14}	S15
$(4N4)_2AgBiBr_8$	2.5	18.8 ± 0.2	6360 ± 58	1.1 (± 0.02) $\times 10^9$	This work
$(4N4)_2AgSbBr_8$	2	8.6 ± 0.2	2880 ± 25	0.8 (± 0.02) $\times 10^9$	This work
$(6N6)_2AgBiBr_8$	1.5	16.1 ± 0.2	5418 ± 90	1.9 (± 0.1) $\times 10^9$	This work

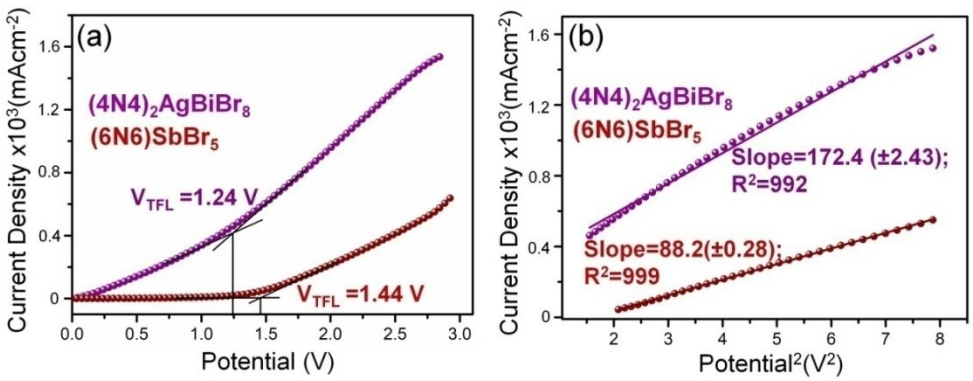

Figure S22. (a) Dark *J-V* and (b) $J\text{-}V^2$ plots for $(4N4)_2AgBiBr_8$ and $(6N6)SbBr_5$ hole-only devices.

Table S12. RT, FT and different impedance components (R_s, R_{CO} and R_{CT}) for $(4N4)_2AgBiBr_8$ and $(4N4)_2AgSbBr_8$ under self-powered condition at 50 $mWcm^{-2}$.

Perovskite	RT (ms)	FT (ms)	R_s (Ω)	R_{CO} (Ω)	R_{CT} (Ω)
$(4N4)_2AgBiBr_8$	98	95	21 ± 2	-	2902 ± 17
$(4N4)_2AgSbBr_8$	104	98	39 ± 2	3464 ± 17	26171 ± 1036

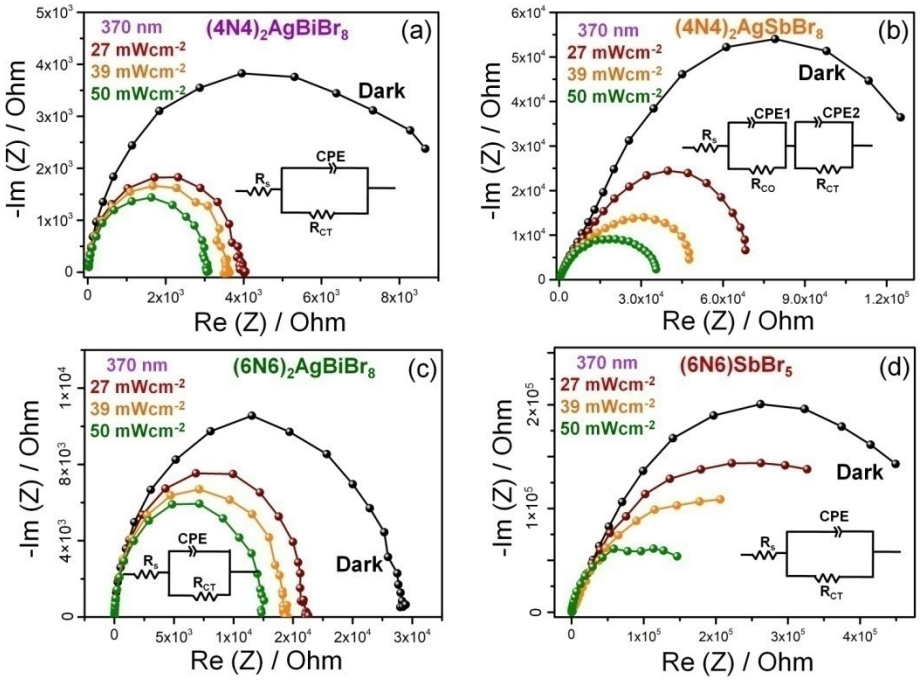

Figure S23. Nyquist plots of (a) $(4N4)_2AgBiBr_8$, (b) $(4N4)_2AgSbBr_8$, (c) $(6N6)_2AgBiBr_8$, and (d) $(6N6)SbBr_5$ in the presence of UV light with different intensities. Insets show the corresponding equivalent circuits.

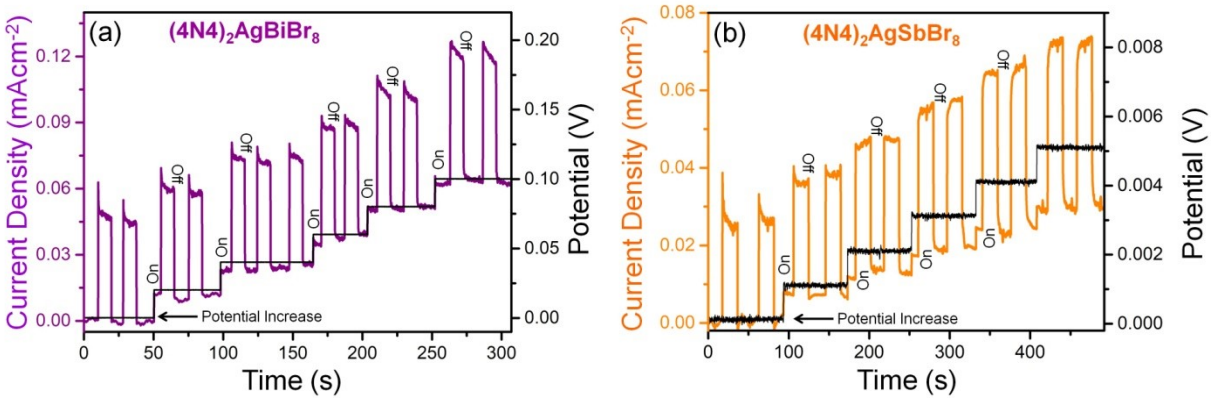

Figure S24. Chronoamperometry and *V-t* plots of (a) $(4N4)_2AgBiBr_8$ and (b) $(4N4)_2AgSbBr_8$ photodetectors.

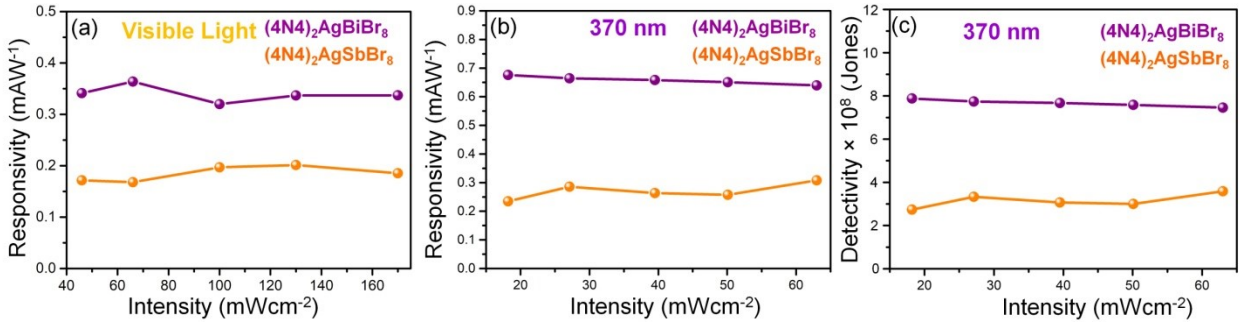

Figure S25. Variation of responsivity with light intensity in the presence of (a) visible light (b) UV light (370 nm) for $(4N4)_2AgBiBr_8$ and $(4N4)_2AgSbBr_8$ devices at 0 V. (c) Variation of detectivity for the photodetectors in presence of UV light with different intensities.

Table S13. Highest responsivity (*R*), detectivity (*D*) values of the $(4N4)_2AgBiBr_8$ and $(4N4)_2AgSbBr_8$under self-powered mode.

Perovskite	R (mAW^{-1}) (Visible)	R (mAW^{-1}) (370 nm)	D (Jones) (370 nm)
$(4N4)_2AgBiBr_8$	3.6 (± 0.08) × 10^{-1}	6.7 (± 0.01) × 10^{-1}	7.7 (± 0.2) × 10^8
$(4N4)_2AgSbBr_8$	2 (± 0.04) × 10^{-1}	2.9 (± 0.02) × 10^{-1}	3.2 (± 0.4) × 10^8

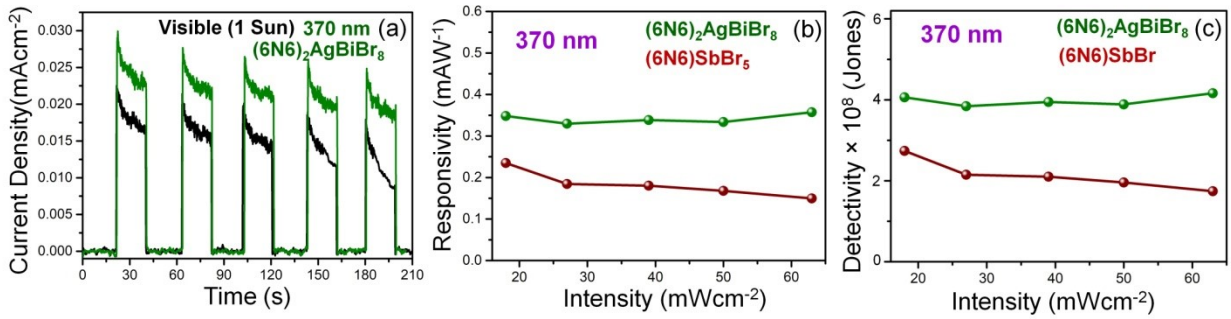

Figure S26. (a) Chronoamperometry plots of $(6N6)_2AgBiBr_8$ under 1 sun visible light and UV light (370 nm) in self-powered mode. Variation of (b) responsivity and (c) detectivity with different intensities of UV light (370 nm) for $(6N6)_2AgBiBr_8$ and $(6N6)SbBr_5$ devices.

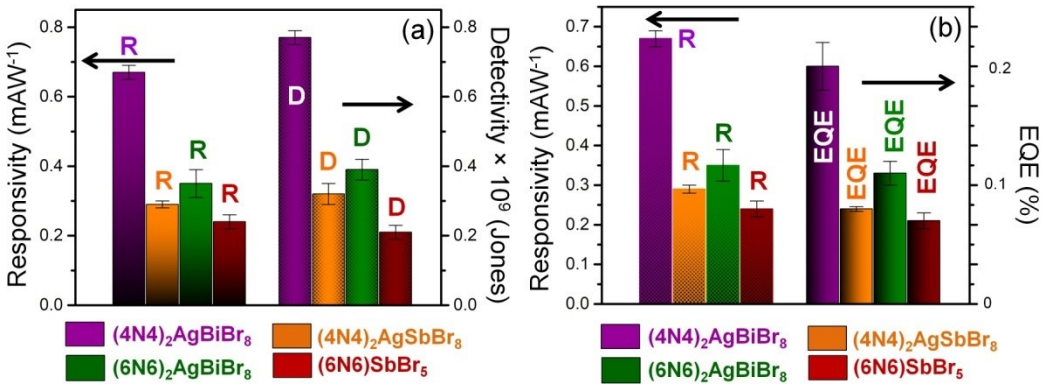

Figure S27. Bar plots of the highest (a) responsivity (*R*) and detectivity (*D*), and (b) *R* and *EQE* for all the bromide DJ-HLDP and 1D $(6N6)SbBr_5$ under self-powered mode.

Table S14. Highest obtained photodetection parameters for all the bromide photodetectors under self-powered mode (0 V).

Perovskite	responsivity (mAW^{-1})	detectivity (Jones)	EQE (%)
$(4N4)_2AgBiBr_8$	6.7 (± 0.1) × 10^{-1}	7.7 (± 0.2) × 10^{8}	2 (± 0.03) × 10^{-1}
$(4N4)_2AgSbBr_8$	2.9 (± 0.2) × 10^{-1}	3.2 (± 0.4) × 10^{8}	8.7 (± 0.02) × 10^{-2}
$(6N6)_2AgBiBr_8$	3.5 (± 0.4) × 10^{-1}	3.9 (± 0.4) × 10^{8}	1.1 (± 0.1) × 10^{-1}
$(6N6)SbBr_5$	2.4 (± 0.2) × 10^{-1}	2.1(± 0.4) × 10^{8}	7.9 (± 0.07) × 10^{-2}

Table S15. RT, FT and different impedance components (R_s, R_{CO} and R_{CT}) for all the bromide photodetector devices under self-powered mode (0V) at 50 $mWcm^{-2}$.

Perovskite	RT (ms)	FT (ms)	R_s (Ω)	R_{CO} (Ω)	R_{CT} (Ω)
$(4N4)_2AgBiBr_8$	98	95	21 ± 2	-	2902 ±17
$(4N4)_2AgSbBr_8$	104	98	39 ± 2	3464 ± 17	26171 ± 1036
$(6N6)_2AgBiBr_8$	100	99	20 ± 2	-	12520 ± 32
$(6N6)SbBr_5$	99	100	27 ± 1	29104 ± 270	147043 ± 3338

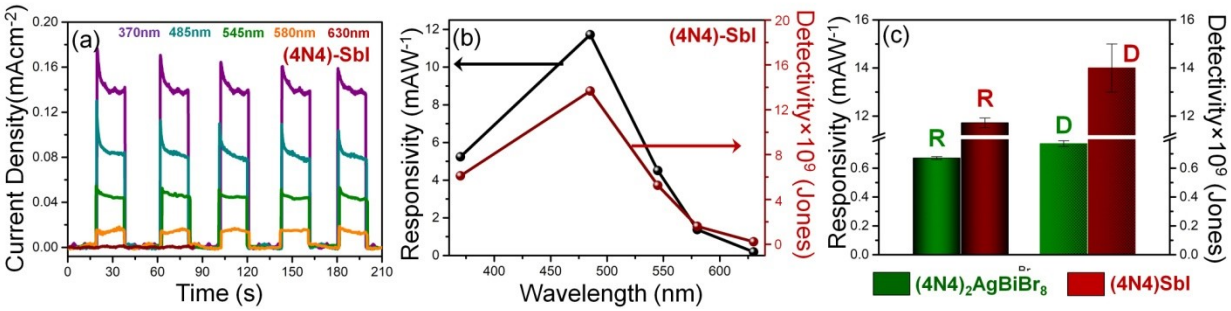

Figure S28. (a) Wavelength-dependent chronoamperometry plots of (4N4)-SbI devices. (b) Variation of responsivity and detectivity with wavelength for (4N4)-SbI devices. (c) Bar plots for

the comparison of highest responsivity and detectivity of $(4N4)_2AgBiBr_8$ and (4N4)-SbI in self-powered mode.

Table S16. Highest obtained photodetection parameters of the $(4N4)_2AgBiBr_8$ and (4N4)-SbI devices under self-powered mode.

Perovskite	wavelength (nm)	responsivity (mAW^{-1})	detectivity (Jones)	*EQE* (%)
$(4N4)_2AgBiBr_8$	370	6.7 (± 0.1) × 10^{-1}	7.7 (± 0.2) × 10^{8}	2 (± 0.03) × 10^{-1}
(4N4)-SbI	485	11.7 (± 0.2)	1.4 (± 0.1) × 10^{10}	3.9 (± 0.05)

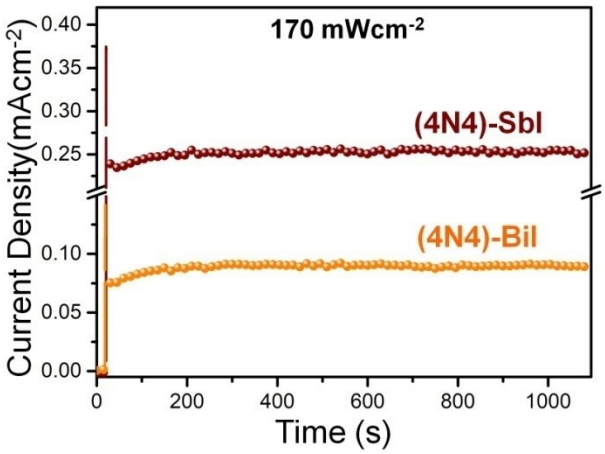

Figure S29. Chronoamperometry plots of the (4N4)-BiI and (4N4)-SbI photodetectors for stability test in the presence of 170 $mWcm^{-2}$ light intensity.

Supporting References

S1 W. Zhang, M. Hong and J. Luo, *Angew. Chem. Int. Ed.* 2020, **132**, 9391-9394.
S2 Y. Li, T. Yang, Z. Xu, X. Liu, X. Huang, S. Han, Y. Liu, M. Li, J. Luo and Z. Sun, *Angew. Chem. Int. Ed.* 2020, **132**, 3457-3461.
S3 D. Li, X. Liu, W. Wu, Y. Peng, S. Zhao, L. Li, M. Hong and J. Luo, *Angew. Chem. Int. Ed.* 2021, **133**, 8496-8499.
S4 Z. Lai, R. Dong, Q. Zhu, Y. Meng, F. Wang, F. Li, X. Bu, X. Kang, H. Zhang, Q. Quan, W. Wang, F. Wang, S. Yip and J. Ho, *ACS Appl. Mater. Interfaces* 2020, **12**, 39567-39577.
S5 D. Fu, J. Yuan, S. Wu, Y. Yao, X. Zhang and X. Zhang, *Inorg. Chem. Front.* 2020, **7**, 1394-1399.
S6 D. Fu, Z. Hou, Y. He, H. Wu, S. Wu, Y. Zhang, G. Niu and X.-M. Zhang, *ACS Appl. Mater. Interfaces* 2022, **14**, 11690-11698.
S7 D. Fu, S. Wu, J. Xin, X. Zhang, G. Han and X. Zhang, *Chem. Commun.* 2020, **56**, 14381-14384.
S8 Z. Wang, X. Zhang, H. Ye, T. Zhu and J. Luo, *Chem. Eur. J.* 2022, **28**, e2022008.
S9 T. Yang, Y. Li, S. Han, Z. Xu, Y. Liu, X. Zhang, X. Liu, B. Teng, J. Luo and Z. Sun, *Small* 2020, **16**, 1907020.
S10 Z. Lai, F. Wang, Y. Meng, X. Bu, X. Kang, Q. Quan, W. Wang, C. Liu, S. P. Yip and J. C. Ho, *Adv. Opt. Mater.* 2021, **9**, 2101523.
S11 L.-Z. Lei, Z.-F. Shi, Y. Li, Z.-Z. Ma, F. Zhang, T.-T. Xu, Y.-T. Tian, D. Wu, X.-J. Li and G.-T. Du, *J. Mater. Chem. C* 2018, **6**, 7982-7988.
S12 F. Fang, Y. Wan, H. Li, S. Fang, F. Huang, B. Zhou, K. Jiang, V. Tung, L.-J. Li and Y. Shi, *ACS Nano* 2022, **16**, 3985-3993.
S13 D. Hao, D. Liu, S. Zhang, L. Li, B. Yang and J. Huang, *Adv. Opt. Mater.*2022, **10**, 2100786.
S14 Y. Dang, G. Tong, W. Song, Z. Liu, L. Qiu, L. K. Ono and Y. Qi, *J. Mater. Chem. C* 2020, **8**, 276-284.
S15 F. Fang, H. Li, S. Fang, B. Zhou, F. Huang, C. Ma, Y. Wan, S. Jiang, Y. Wang, B. Tian and Y. Shi, *Adv. Opt. Mater.* 2021, **9**, 2001930.